A Seismo-Acoustic Analysis of the 2017 North Korean Nuclear Test

all authors contributed equally.

Jelle Assink,

R&D Seismology and Acoustics, Royal Netherlands Meteorological Institute (KNMI),

P.O. Box 201, 3730 AE, De Bilt, The Netherlands, assink@knmi.nl

Gil Averbuch,

Faculty of Civil Engineering and Geosciences, Department of Geoscience and Engineering,

Delft University of Technology, Stevinweg 1, 2628 CN, Delft, The Netherlands

Shahar Shani-Kadmiel,

Faculty of Civil Engineering and Geosciences, Department of Geoscience and Engineering,

Delft University of Technology, Stevinweg 1, 2628 CN, Delft, The Netherlands

Pieter Smets,

Faculty of Civil Engineering and Geosciences, Department of Geoscience and Engineering,

Delft University of Technology, Stevinweg 1, 2628 CN, Delft, The Netherlands

Läslo Evers,

Seismology and Acoustics, Royal Netherlands Meteorological Institute (KNMI),

P.O. Box 201, 3730 AE, De Bilt, The Netherlands

Faculty of Civil Engineering and Geosciences, Department of Geoscience and Engineering,

Delft University of Technology, Stevinweg 1, 2628 CN, Delft, The Netherlands

Abstract

The 2017 North Korean nuclear test gave rise to seismic and low-frequency acoustic signals, i.e. infrasound. The infrasonic signals are due to seismo-acoustic coupling and have been detected on microbarometer array I45RU in the Russian Federation at 401 km from the test site. I45RU is part of the International Monitoring System for the verification of the Comprehensive Nuclear-Test-Ban Treaty. We analyze the seismo-acoustic coupling by making use of array processing and back-projection techniques. The back-projections show that infrasound radiation is not confined to the epicentral region. More distant regions are found to be consistent with locations of topography, sedimentary basins, and underwater evanescent sources. The back-projections can be used to estimate the average infrasonic propagation speed through the atmosphere. We discuss these findings in the context of infrasound propagation conditions during the sixth nuclear test. It is suggested that propagation from the test site to I45RU may have occurred along unexpected paths instead of typical stratospheric propagation. We present several scenarios that could be considered in the interpretation of the observations.

Keywords: infrasound, array processing, back-projections, DPRK, Earthquake monitoring and test-ban treaty verification, wave propagation

I Introduction

The Democratic People's Republic of Korea (DPRK) has performed six underground nuclear tests since 2006. Seismic signals from these tests have been detected globally and have been used to estimate the epicenter, origin time and seismic magnitude. The seismic measurements indicate that the DPRK has tested larger nuclear weapons over time. The facilities of the International Monitoring System (IMS), which is in place for the verification of the Comprehensive Nuclear-Test-Ban Treaty (CTBT), have been instrumental in the accurate localization and characterization of the tests (e.g., Gibbons et al. (2017)). The yield estimate of the explosions strongly trades-off with their depth, which is difficult to estimate from teleseismic arrivals alone (Bowers and Selby, 2009).

Large seismic sources also generate observable infrasound in the atmosphere. The coupling of seismic waves to atmospheric infrasound waves can occur due to various mechanisms. Generation of acoustic waves from surface waves in a solid-fluid system is a well-known phenomenon (Scholte, 1947; Stoneley, 1926). It has been shown that air-coupled surface waves also contribute to the observed acoustic signal in the atmosphere (Ben-Menahem and Singh, 1981; Ewing et al., 1957). It follows that the solid earth-atmosphere and ocean-atmosphere interfaces are transparent for the inhomogeneous part of the wave field as this spectrum includes low phase velocities that are evanescent in the solid earth or oceans, but can be propagating in the atmosphere (Godin, 2008, 2011). Evanescently coupled infrasound has been observed from the 2004 Mw8.1 Macquarie ridge earthquake, as acoustic signals with relatively large wavelengths coupled from shallow underwater features (Evers et al., 2014).

Previous studies of infrasound from earthquakes have shown that most of the coupled

seismo-acoustic signals originate from the epicentral region. This is referred to as epicentral infrasound. In addition, secondary infrasonic signals have been observed from the movement of mountain ranges, away from the epicenter (Green et al., 2009; Le Pichon et al., 2003; Young and Greene, 1982). In an analysis of the 2016 Central Italy earthquakes, it was shown that seismo-acoustic coupling occurs over an even larger extent. The detection of these signals was dependent on the ground-to-air coupling and atmospheric propagation conditions to a distant array (Shani-Kadmiel et al., 2018).

The detection of infrasound at a remote station is strongly dependent on the noise levels due to the local wind and turbulence and the propagation conditions along the source-receiver path. Long-range infrasound propagation, i.e. propagation over distances longer than 100 km, is facilitated by atmospheric waveguides. These waveguides are formed between the ground and atmospheric layers aloft and are much dependent on the prevailing vertical temperature and wind distribution. The stratospheric waveguide is particularly important in the detection of long-range infrasound and is sustained by a strong wind jet around 50 km altitude, i.e. the stratospheric vortex. As the direction of the flow reverses during the equinoxes, the propagation efficiency of the stratospheric waveguide reduces. A thermospheric waveguide always exists because of a strong temperature gradient in the lower thermosphere. The low density in the upper atmosphere leads to non-linear propagation effects and significant absorption (e.g., Lonzaga et al. (2014); Waxler et al. (2017)).

Previous underground nuclear tests by the DPRK have generated infrasound that has been observed on IMS stations (Assink et al., 2016) and infrasound arrays in South Korea (Che et al., 2014). As seismo-acoustic coupling is related to source depth, this motivates a synergy between seismology and acoustics, e.g. to improve depth-yield estimates of (nuclear)

explosions. The effect of source depth on seismo-acoustic coupling has been studied previously (Arrowsmith et al., 2011; Ford et al., 2014). Assink et al. (2016) hypothesized that a relative source depth between two events can be estimated from infrasonic observations. In this procedure, 1) the coupling of seismic waves to infrasound is quantified and 2) the propagation paths are known in order to estimate the relative transmission loss from the Earth surface to the receiver.

In this article, we focus on a seismo-acoustic analysis of the 03 September 2017 nuclear test. Besides a main event at 03:30:01 UTC, a non-tectonic aftershock occurred at 03:38:32 in the vicinity of the test site, possibly related to collapse of the underground cavity (Liu et al., 2018). The source characteristics are summarized in Table 1 and are derived with seismic stations from the IMS. Infrasound was detected on a nearby IMS infrasound array in the Russian Federation, I45RU (see Figure 1), as well as in South-Korea. This analysis focuses on seismo-acoustic signals that have been detected on I45RU. This array is located at a distance of 401 km distance to the northeast of the Punggye-ri Nuclear Test Site. We show that array processing and back-projections using recorded data from this IMS array provide unprecedented insight into seismo-acoustic coupling.

Furthermore, we discuss the infrasound propagation conditions during the sixth nuclear test, during which the stratosphere was in a state of transition from summer to winter and the stratospheric vortex was relatively weak. As long-range infrasound propagation is largely conditioned by the strength and the direction of the stratospheric vortex, this implies that propagation from the test site to I45RU may have occurred along unexpected paths (Chunchuzov et al., 2015; Green et al., 2011; Kulichkov, 2010). We present several scenarios that could be considered in the interpretation of the observations.

II Data acquisition and processing

I45RU is a triangular array with a central element and has an aperture of 2.1 km. The array is equipped with four MB2000 absolute microbarometers that have a flat frequency response between 0.01-8 Hz. A rosette wind-noise reduction system is used to reduce wind noise over the infrasonic frequency band by spatially averaging the pressure field in the vicinity of each infrasound sensor. The MB2000 sensors sample the pressure field at 20 Hz. The microbarometers are primarily sensitive to pressure fluctuations but appear to be responsive to mechanical vibrations as well (Alcoverro et al., 2005). The sensitivity to both seismic and acoustic waves has been discussed in previous seismo-acoustic analyses of larger earthquakes (e.g., Le Pichon et al. (2003); Shani-Kadmiel et al. (2018)).

We use time-domain (Melton and Bailey, 1957) and frequency-domain (Smart and Flinn, 1971) beamforming techniques for the detection of coherent infrasound and the estimation of plane wave parameters, i.e. back azimuth and apparent velocity. The detection of a signal is based on the evaluation of a Fisher ratio. The probability of detection can be estimated through the statistical framework of Fisher statistics. Moreover, a single-channel SNR value can be estimated from the Fisher ratio. A detailed description of these algorithms can be found in Evers (2008).

The waveform data is detrended and band-pass filtered before time-domain beamforming. A second order Butterworth band-pass filter between 0.35 to 4 Hz appears to be a good trade-off between the coherency of the signals of interest and interference from low-frequency noise, such as coherent noise in the microbarom band. In addition, a 1.0-3.0 Hz frequency band is considered in order to detect smaller amplitude arrivals that would otherwise be

masked. The waveforms are oversampled to 100 Hz using Fourier interpolation for an enhanced time resolution as smaller time shifts may be used. This enhanced time resolution benefits the beamforming of the seismic arrivals.

The frequency-domain algorithm carries out the analysis in discrete frequency bands. The window size is 20 and 40 seconds for the time-domain and frequency domain processing, respectively. In all cases, we consider 90% overlap between successive windows. The samples are delayed and summed over a horizontal slowness grid. The grid is designed to include back azimuth and apparent velocity values of interest. The back azimuth values range between 155 to 270 degrees and are spaced by 1 degree. The lower limit of 155 degrees is selected to avoid detection of microbarom sources in the Pacific. The apparent velocity values range between 300 m/s and 10 km/s. Between 300 m/s and 450 m/s the values are separated by 5 m/s (the infrasonic signal range), and between 450 m/s and 10 km/s the values are logarithmically spaced (the seismic signal range).

III Array processing and waveform analysis

Figure 2 shows array processing results for I45RU between 03:30:00 and 04:05:00. From top to bottom, the frames show as a function of time: apparent velocity, back azimuth, best beam and coherency as a function of frequency. Detections with a SNR above 0.6 are colored conforming to the color map. Travel time and celerity (defined as the epicentral distance divided by the traveltime) are indicated on the lowest frame and are relative to the origin time. A first interpretation of the arrival structure follows from these celerity values.

Figure 2a shows the arrival of various coherent arrivals in the 0.35-4.0 Hz frequency band from the direction of the test site, indicated by the dashed horizontal line. The wave train

between 57 and ˜300 seconds corresponds to the seismic arrivals. The first P-wave arrives after 57 seconds, which is in agreement with the iasp91 seismic travel time tables (Kennett et al., 1995). After the high-frequency P-wave, a dispersive Lg wave group is detected, which represents a guided waveform with predominantly transverse particle motion. The measured apparent velocities are consistent with seismic propagation velocities. The seismic waves radiate infrasound vertically into the atmosphere, which is measured by the microbarometer (e.g., Cook (1971)). However, part of this measurement is a contribution from the mechanical sensitivity of the MB2000 (Alcoverro et al., 2005), for the larger accelerations between 57 and ˜130 s.

The second set of arrivals from the direction of the test site corresponds to infrasound waves that have propagated through the atmosphere, having typical celerity values between 0.23 and 0.34 km/s and apparent velocities around 340 m/s. These infrasonic arrivals are interpreted to be epicentral infrasound. The resolved back azimuth and apparent velocity values show significant variations along the mostly emergent wave train. Most of the energy is coherent in a frequency range between 0.35 to 1.5 Hz.

Within this wave train, two phases, which are detailed in Figure 3, stand out: (1) An oscillatory wave package with a duration of ˜20 seconds, arriving after 1440 seconds with a dominant frequency around 0.4 Hz and a peak-to-peak (ptp) amplitude of 0.3 Pa. (2) A broadband signal arriving after 1510 seconds, coherent between 0.05 to 4 Hz and a ptp amplitude of 0.75 Pa. The broadband signal consists of higher frequencies that are superimposed on a low-frequency (˜0.1 Hz) U-wave. The shape of this signal matches the classical shape of thermospheric return signals as described in many cases in the scientific literature (Assink, 2012; Lonzaga et al., 2014; Whitaker and Mutschlecner, 2008).

Another arrival, labeled (3) in Figure 3, is observed around 2025 seconds after the main event, with a dominant frequency around 0.25 Hz and a ptp amplitude of 0.15 Pa. The back azimuth is consistent with the direction of the test site and apparent velocities are consistent with an acoustic signal. When associated with the non-tectonic aftershock, this late arrival has a similar travel time (indicated by horizontally spanning arrows in Figure 2a) as arrival (2) does with respect to the main event, suggesting it has propagated along a similar path.

Figure 2b shows the array processing results in the 1.0-3.0 Hz band. In between 600 and 1300 seconds, coherent infrasound is detected that is predominantly coherent between 1.0-2.0 Hz. As such, these arrivals have celerity values between 0.6 and 0.34 km/s and appear before the epicentral infrasound. Compared to the epicentral infrasound, these arrivals have much smaller amplitudes and arrive from a different back azimuth. The resolved back azimuth is 208°, whereas the test site is at 218°. Similar signals have been identified in previous studies on infrasound from large earthquakes, as secondary infrasound (Le Pichon et al., 2003; Marchetti et al., 2016; Shani-Kadmiel et al., 2018). To understand where seismo-acoustic coupling occurs, array processing results are back-projected following the method described in Shani-Kadmiel et al. (2018).

IV Back-projections

Detections shown in Figure 2 are back-projected assuming a constant seismic and infrasonic propagation velocities. Due to the order of magnitude difference between seismic and infrasonic propagation velocities, this procedure is much more sensitive to the latter than the former. It is therefor fairly safe to approximate the seismic propagation velocity by fixing it around the celerity value of the peak amplitude arrival of the seismic wave train and to

test a range of infrasonic propagation velocities. For the purpose of this study we fixed the seismic propagation velocity to 6 km/s. In contrast to seismic propagation velocities, infrasonic propagation velocities are constrained to a relatively small range between 220 m/s and 340 m/s. In this range, 0.28 km/s was found to provide the best overlap with respect to epicentral location, topographic features, and potential sources of evanescent wave coupling (Figure 4). It also matches the celerity value for the peak amplitude arrival of the infrasonic signal and is in agreement with expected celerities of thermospheric returns.

A grid of theoretical source to receiver travel times (seismic + infrasonic) and back azimuths is constructed with a 0.05° spacing. Time of arrival and back-azimuth associated with each detection point arriving more than 600 seconds after origintime with SNR > 0.7 and apparent velocity in the 280 m/s to 450 m/s range, are used to locate the grid cell from which it most likely originated. The contribution of each detection to the count of detections originating in each cell is the associated SNR value; For example, two detections originating from the same grid cell, one with SNR=1 and another with SNR=0.8 will result in a count of 1.8. This approach does not account for any horizontal advection due to crosswind and along track wind, which may result in inaccurate locations. However, as described in the next section, during low wind conditions such as in this case, infrasound propagation is predominantly controlled by the temperature structure. Thus, we expect errors related to horizontal advection to be negligible.

Figure 4 shows back-projection results from both frequency bands shown in Figure 2. The wide-band back-projection (Figure 4a) illuminates an elongated infrasound radiation patch along the trend of the Hamgyong mountain range (see Figure 1 for location) with its maximum surrounding the test site. In the narrow-band back-projections, smaller patches of

increased infrasound radiation within the mountain range suggest areas of more efficient radiation to station I45RU exist at this time (Figure 4b). Additionally, infrasound is detected from the Tumen River delta (see Figure 1 for location) about half way between the test site and I45RU. Marchetti et al. (2016) and Shani-Kadmiel et al. (2018) made similar observations of anomalous infrasonic radiation atop alluvial basins due to the interaction of seismic waves with the unconsolidated sediments. Interestingly, this area is not illuminated in the wide-band back-projections, presumably because seismic wave interaction with the shallow unconsolidated sediments of the Tumen River delta is likely to generate higher frequencies and in turn radiate infrasound in the higher frequency band. Infrasound is also detected from over the Japan Basin east of the test site. This basin is within 1 hydroacoustical wavelength of the water-air interface, suggesting evanescent wave coupling. Seismic wave interaction with seamounts protruding from the Japan basin generates higher frequencies. However, evanescent wave coupling may still occur as these are closer to the water-air interface. These effects are illustrated by our back-projection results in Figure 4. Contour lines in Figure 4 correspond to a depth of 1 acoustical wavelength at a range of frequencies calculated as $d_i = c_H/f_i$, with c_H the hydroacoustic speed of sound taken to be 1550 m/s.

V Infrasound propagation during a weak stratospheric vortex

For the analysis of infrasonic propagation conditions, we have compared the European Centre for Medium-range Weather Forecasts (ECMWF) operational high resolution ensemble of analyses (HRES EDA) (Smets et al., 2015) with the MSIS-00 and HWM14 empirical models (Figure 5). The vertical structure of the atmosphere in the region of interest is characterized by a typical eastward jetstream (maximum wind velocity of 16.5 m/s at 11 km) and a weak

westward stratospheric vortex (average wind velocity of 5.8 +/-0.5 m/s between 17-50 km) with a maximum in the stratopause (21.6 m/s at 55 km). Above 65 km, no synoptic state is represented by the climatologies: vertically narrow mesospheric inversion layers (MILs), intense wind shears, and sporadic layers are not present.

Since the nuclear test occurred near the autumnal equinox, planetary waves can reach a zero-wind condition in the middle atmosphere (stratosphere - mesosphere, Figure 5a) enhancing turbulence and small-scale wave activity. MILs typically form near the mesopause throughout the year and near the middle mesosphere during equinox and winter solstice periods (Brown et al., 2004). Small-scale structure and wind shear layers can occur e.g. due to (the breaking of) gravity waves (Yue et al., 2010).

From the effective sound speed profile (Figure 5b), it follows that only a thermospherically ducted arrival is supported (Figure 5c). The effective sound speed is defined as the sum of the adiabatic sound speed and the wind speed in the direction of propagation. Estimates of travel time (1507 seconds, indicated by a vertical blue line in Figure 3), back-azimuth and apparent velocity from ray tracing are in first-order agreement with the observed low-frequency arrival at 1510 seconds after the explosion. This arrival has propagated through the mesosphere and lower thermosphere where non-linear propagation effects are significant. This non-linearity distorts the frequency content of the signal through signal lengthening and wavefront steepening. There is an interplay between these non-linear effects and attenuation as lengthening mitigates against signal attenuation while attenuation limits shock formation (Lonzaga et al., 2014). Indeed, this particular arrival is coherent down to 0.05 Hz.

However, this propagation path does not explain all the observed infrasound at I45RU, as infrasonic arrivals with high celerities, higher frequency content and other azimuths are

also observed. These arrivals could be explained by a combination of various mechanisms (Figure 5c), including:

- Scattering and (partial) reflections off small scale structure and wind shear layers (e.g., Chunchuzov et al. (2015); Kulichkov (2010). Moreover, higher frequencies are more likely to reflect off such structures.

- Propagation along the Earth surface by coupled seismo-acoustic modes. This could be reflected by the similarity in the frequency spectrum between the Lg phase and the bulk of the infrasonic arrivals.

- Evanescent wave coupling from a shallow, low-frequency source. Interaction of radiated energy, from both evanescent and surface waves can keep the energy trapped near the surface and propagate over long distances.

- Uncertainties in atmospheric models or assimilation of data below the mesosphere is possible (e.g., Smets et al. (2016)). However simultaneous observations of Pacific microbaroms at the time of the nuclear tests indicates that the stratospheric vortex was indeed weak, yielding thermospheric ducting (see Supplemental Information).

Finally, the mathematical and physical approximations that are made in the derivation of the propagation modeling techniques should be considered.

VI Discussion and Conclusions

Array processing of recorded pressure fluctuations at IMS array I45RU, 401 km northeast of the Punggye-ri Nuclear Test Site show seismic and infrasonic signals related to the nuclear test. Seismic arrivals are detected with a back azimuth that corresponds to the direction of

the test site. Epicentral infrasound with acoustic apparent velocities and celerities in the range 0.34 to 0.24 km/s are also detected as a result of the nuclear test.

Back-projections using the above detections in two frequency (wide- and narrow-) bands reveals sources of infrasound radiation. Four infrasound sources are identified: (1) The epicentral region, (2) The Hamgyong mountain range, (3) The Tumen River delta, and (4) The Japan Basin and the seamounts protruding from it. The narrow-band back-projections illuminates different regions. This perhaps has the potential to discriminate between sources of infrasound. We defer this investigation to future studies.

A weak stratospheric vortex occurs twice a year during vernal and autumnal equinox as well as at the onset and recovery of Sudden Stratospheric Warming (SSW) events. During this time the paradigm of classical infrasound propagation paths in the middle atmosphere is challenged. During the 2017 test, the structure of the speed of sound in the atmosphere is mostly attributed to the temperature structure with little direct contribution from wind. However, turbulence and small-scale wave activity enhance during these low-wind conditions increasing the importance of scattering and (partial) reflections and the need for synoptic upper atmospheric specifications.

Although the use of infrasound in the estimation of source depth has been previously discussed, a depth analysis has not been considered here due to the unexpected propagation paths.

Data and resources: The CTBTO and ECMWF data used for this paper are available to member states but can be requested for academic purposes. The CTBTO and IMS station operators are thanked for the high-quality data and products. Infrasound data can be requested at the CTBTO International DataCenter (IDC) in Vienna, via the virtual Data Exploration Center. Atmospheric data can be requested at the ECMWF via the Meteorological Archival and Retrieval System (MARS).

Acknowledgements: The contributions by Shahar Shani-Kadmiel, Pieter Smets and Läslo Evers are funded through a VIDI project from the Netherlands Organization for Scientific Research (NWO), project 864.14.005. Gil Averbuch is funded through the Marie Curie Action WAVES from the EuropeanUnion within H2020, grant number 641943. Figures in this article are made with Matplotlib version 2.1.0 (Hunter, 2007) and Generic Mapping Tools (Wessel et al., 2013).

REFERENCES

Alcoverro, B., Marysevich, P., and Starovoit, Y. (2005). Mechanical Sensitivity of Microbarometers MB2000 (DASE, France) and Chaparral5 (USA) to Vertical and Horizontal Ground Motion. *Inframatics: The newsletter of subaudible sound*, 9(09):1–10.

Arrowsmith, S., Whitaker, R., and Stead, R. (2011). Infrasound as a Depth Discriminant. In *Proceedings of the 2011 Monitoring Research Review - Ground-Based Nuclear Explosion Monitoring Technologies, 13-15 September 2011, Tucson, AZ*, pages 755–765.

Assink, J. D. (2012). *Infrasound as upper atmospheric monitor*. Phd thesis, University of Mississippi.

Assink, J. D., Averbuch, G., Smets, P. S. M., and Evers, L. G. (2016). On the infrasound detected from the 2013 and 2016 DPRK ' s underground nuclear tests. *Geophysical Research Letters*, 43:3526–3533.

Ben-Menahem, A. and Singh, S. J. (1981). *Seismic Waves and Sources*. Springer Verlag, New York, New York, USA, 1st edition.

Bowers, D. and Selby, N. D. (2009). Forensic Seismology and the Comprehensive Nuclear-Test-Ban Treaty. *Annual Review of Earth and Planetary Sciences*, 37(1):209–236.

Brown, L. B., Gerrard, A. J., Meriwether, J. W., and Makela, J. J. (2004). All-sky imaging observations of mesospheric fronts in OI 557.7 nm and broadband OH airglow emissions: Analysis of frontal structure, atmospheric background conditions, and potential sourcing mechanisms. *Journal of Geophysical Research D: Atmospheres*, 109(19):1–19.

Che, I. Y., Park, J., Kim, I., Kim, T. S., and Lee, H. I. (2014). Infrasound signals from the underground nuclear explosions of North Korea. *Geophysical Journal International*, 198(1):495–503.

Chunchuzov, I., Kulichkov, S., Perepelkin, V., Popov, O., Firstov, P., Assink, J. D., and Marchetti, E. (2015). Study of the wind velocitylayered structure in the stratosphere, mesosphere, and lower thermosphere by using infrasound probing of the atmosphere. *Journal of Geophysical Research: Atmospheres*, 120(17):8828–8840.

Cook, R. K. (1971). Infrasound Radiated During the Montana Earthquake of 1959 August 18. *Geophysical Journal of the Royal Astronomical Society*, 26(1-4):191–198.

Evers, L. G. (2008). *The inaudible symphony: On the detection and source identification of atmospheric infrasound*. Phd thesis, Delft University of Technology, The Netherlands.

Evers, L. G., Brown, D., Heaney, K. D., Assink, J. D., Smets, P. S., and Snellen, M. (2014). Evanescent wave coupling in a geophysical system: Airborne acoustic signals from the Mw 8.1 Macquarie Ridge earthquake. *Geophysical Research Letters*, 41(5):1644–1650.

Ewing, W. M., Jardestzky, W. S., and Press, F. (1957). *Elastic waves in layered media*. McGraw-Hill series in the geological sciences. McGraw-Hill, New York, USA, 1st edition.

Ford, S. R., Rodgers, A. J., Xu, H., Templeton, D. C., Harben, P., Foxall, W., and Reinke, R. E. (2014). Partitioning of seismoacoustic energy and estimation of yield and height-of-burst/depth-of-burial for near-surface explosions. *Bulletin of the Seismological Society of America*, 104(2):608–623.

Gibbons, S. J., Pabian, F., Näsholm, S. P., Kværna, T., and Mykkeltveit, S. (2017). Accurate relative location estimates for the North Korean nuclear tests using empirical slowness corrections. *Geophysical Journal International*, 208(1):101–117.

Godin, O. A. (2008). Sound transmission through water-air interfaces: New insights into an old problem. *Contemporary Physics*, 49(2):105–123.

Godin, O. A. (2011). Low-frequency sound transmission through a gassolid interface. *The Journal of the Acoustical Society of America*, 129(2):EL45–EL51.

Green, D. N., Guilbert, J., le Pichon, A., Sebe, O., and Bowers, D. (2009). Modelling ground-to-air coupling for the shallow ML 4.3 Folkestone, United Kingdom, earthquake of 28 April 2007. *Bulletin of the Seismological Society of America*, 99(4):2541–2551.

Green, D. N., Vergoz, J., Gibson, R., Le Pichon, A., and Ceranna, L. (2011). Infrasound radiated by the Gerdec and Chelopechene explosions: Propagation along unexpected paths. *Geophysical Journal International*, 185(2):890–910.

Hunter, J. D. (2007). Matplotlib: A 2D graphics environment. *Computing in Science and Engineering*, 9(3):99–104.

Kennett, B. L. N., Engdahl, E. R., and Buland, R. (1995). Constraints on seismic velocities in the Earth from travel times. *Geophysical Journal International*, 122(June):108–124.

Kulichkov, S. (2010). On the Prospects for Acoustic Sounding of the Fine Structure of the Middle Atmosphere. In Le Pichon, A., Blanc, E., and Hauchecorne, A., editors, *Infrasound Monitoring for Atmospheric Studies*, chapter 16, pages 511–540. Springer, New York, USA.

Le Pichon, A., Guilbert, J., Vallée, M., Dessa, J. X., and Ulziibat, M. (2003). Infrasonic imaging of the Kunlun Mountains for the great 2001 China earthquake. *Geophysical Research Letters*, 30(15):2–5.

Liu, J., Li, L., Zahradník, J., Sokos, E., Liu, C., and Tian, X. (2018). North Korea's 2017 Test and its Nontectonic Aftershock. *Geophysical Research Letters*, 45(7):3017–3025.

Lonzaga, J. B., Waxler, R. M., Assink, J. D., and Talmadge, C. L. (2014). Modelling waveforms of infrasound arrivals from impulsive sources using weakly non-linear ray theory. *Geophysical Journal International*, 200(3):1347–1361.

Marchetti, E., Lacanna, G., Le Pichon, A., Piccinini, D., and Ripepe, M. (2016). Evidence of Large Infrasonic Radiation Induced by Earthquake Interaction with Alluvial Sediments. *Seismological Research Letters*, 87(3):678–684.

Melton, B. S. and Bailey, L. F. (1957). Multiple Signal Correlators. *Geophysics*, 22(3):565–588.

Scholte, J. G. (1947). The Range of Existence of Rayleigh and Stoneley Waves. *Geophysical Supplements to the Monthly Notices of the Royal Astronomical Society*, 5(5):120–126.

Shani-Kadmiel, S., Assink, J. D., Smets, P. S., and Evers, L. G. (2018). Seismoacoustic Coupled Signals From Earthquakes in Central Italy: Epicentral and Secondary Sources of Infrasound. *Geophysical Research Letters*, 45(1):427–435.

Smart, E. and Flinn, E. A. (1971). Fast Frequency-Wavenumber Analysis and Fisher Signal Detection in Real-Time Infrasonic Array Data Processing. *Geophysical Journal of the Royal Astronomical Society*, 26:279–284.

Smets, P. S. M., Assink, J. D., Le Pichon, A., and Evers, L. G. (2016). ECMWF SSW forecast evaluation using infrasound. *Journal of Geophysical Research: Atmospheres*, 121(9):4637–4650.

Smets, P. S. M., Evers, L. G., Näsholm, S. P., and Gibbons, S. J. (2015). Probabilistic infrasound propagation using realistic atmospheric perturbations. *Geophysical Research Letters*, 42:6510–6517.

Stoneley, R. (1926). The Effect of the Ocean on Rayleigh Waves. *Geophysical Journal International*, 1(s7):349–356.

Waxler, R., Assink, J., and Velea, D. (2017). Modal expansions for infrasound propagation and their implications for ground-to-ground propagation. *The Journal of the Acoustical Society of America*, 141(2):1290–1307.

Weatherall, P., Marks, K. M., Jakobsson, M., Schmitt, T., Tani, S., Arndt, J. E., Rovere, M., Chayes, D., Ferrini, V., and Wigley, R. (2015). A new digital bathymetric model of the world's oceans. *Earth and Space Science*, 2:331–345.

Wessel, P., Smith, W. H., Scharroo, R., Luis, J., and Wobbe, F. (2013). Generic mapping tools: Improved version released. *Eos*, 94(45):409–410.

Whitaker, R. W. and Mutschlecner, J. P. (2008). A comparison of infrasound signals refracted from stratospheric and thermospheric altitudes. *Journal of Geophysical Research Atmospheres*, 113(8):1–13.

Young, J. M. and Greene, G. E. (1982). Anomalous infrasound generated by the Alaskan earthquake of 28 March 1964. *J. Acoust. Soc. Am*, 71(March 1964):334–339.

Yue, J., She, C. Y., and Liu, H. L. (2010). Large wind shears and stabilities in the mesopause region observed by Na wind-temperature lidar at midlatitude. *Journal of Geophysical Research: Space Physics*, 115(10):1–12.

	Time	Latitude (deg.)	Longitude (deg.)	m_b magnitude	Est. Yield (kT)
Nuclear Test	03:30:01.08	41.3205	129.0349	6.1	200 - 300
Non-Tectonic Aftershock	03:38:32.08	41.3206	129.0615	4.1	-

Table 1: Details from the events associated with the 2017 North Korean Nuclear Test from the Revised Event Bulletin (REB) published by the CTBT Organization. The yield estimates are estimated by NORSAR, as published at https://www.norsar.no/press/latest-press-release/archive/the-nuclear-explosion-in-north-korea-on-3-september-2017-a-revised-magnitude-assessment-article1548-984.html, last accessed on 30 April 2018.

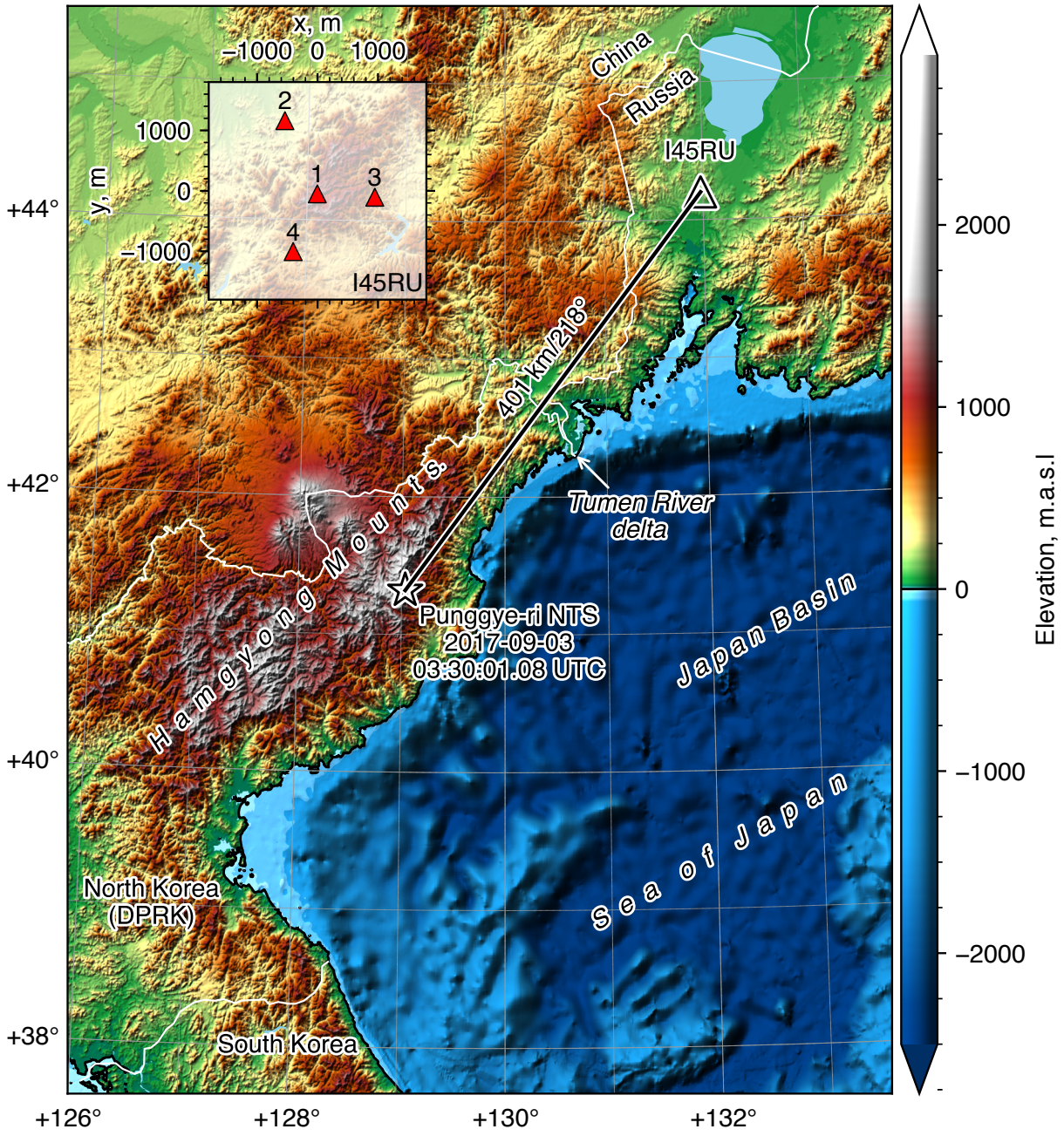

Figure 1: Shaded relief of surface topography and bathymetry from General Bathymetric Chart of the Oceans (GEBCO) 30 arc-second grid (Weatherall et al., 2015). Punggye-ri Nuclear Test Site (NTS) and event epicenter marked by a star and IMS array I45RU marked by a triangle. Hamgyong Mountains and Tumen River delta are marked for further discussion in the text. Inset frame shows I45RU 4 microbarometer configuration.

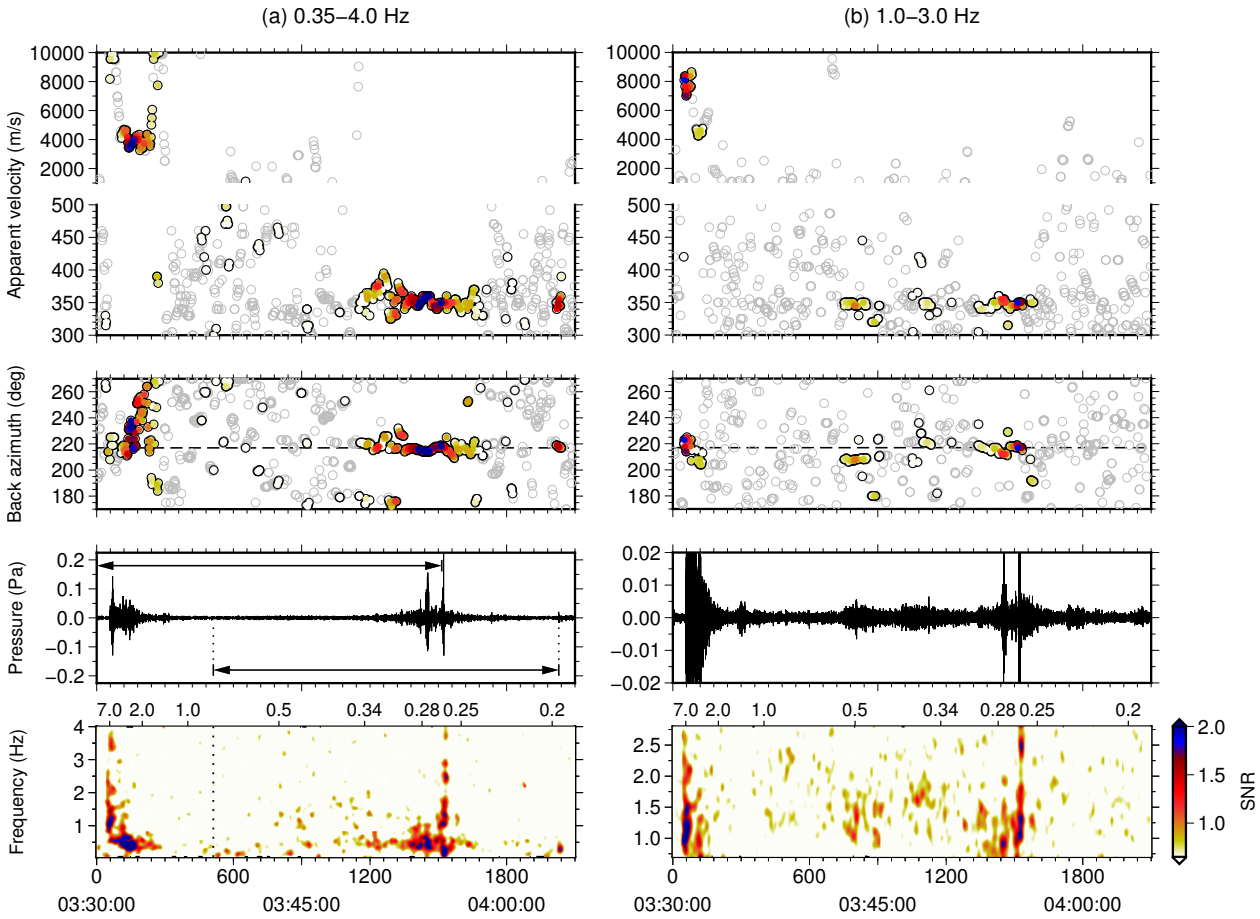

Figure 2: Array processing results (a) 0.35-4.0 Hz wide-band, and (b) 1.0-3.0 Hz narrow band of I45RU between 03:30:00 and 04:05:00 on 3 September 2017. The frames show the following wavefront parameters as a function of time: apparent velocity, back azimuth, best beam, and coherency as a function of frequency. The color scale indicates the signal-to-noise ratio (SNR) of the detection. Travel time in seconds and celerity (in km/s) are indicated on the lowest frame and are relative to the origin time.

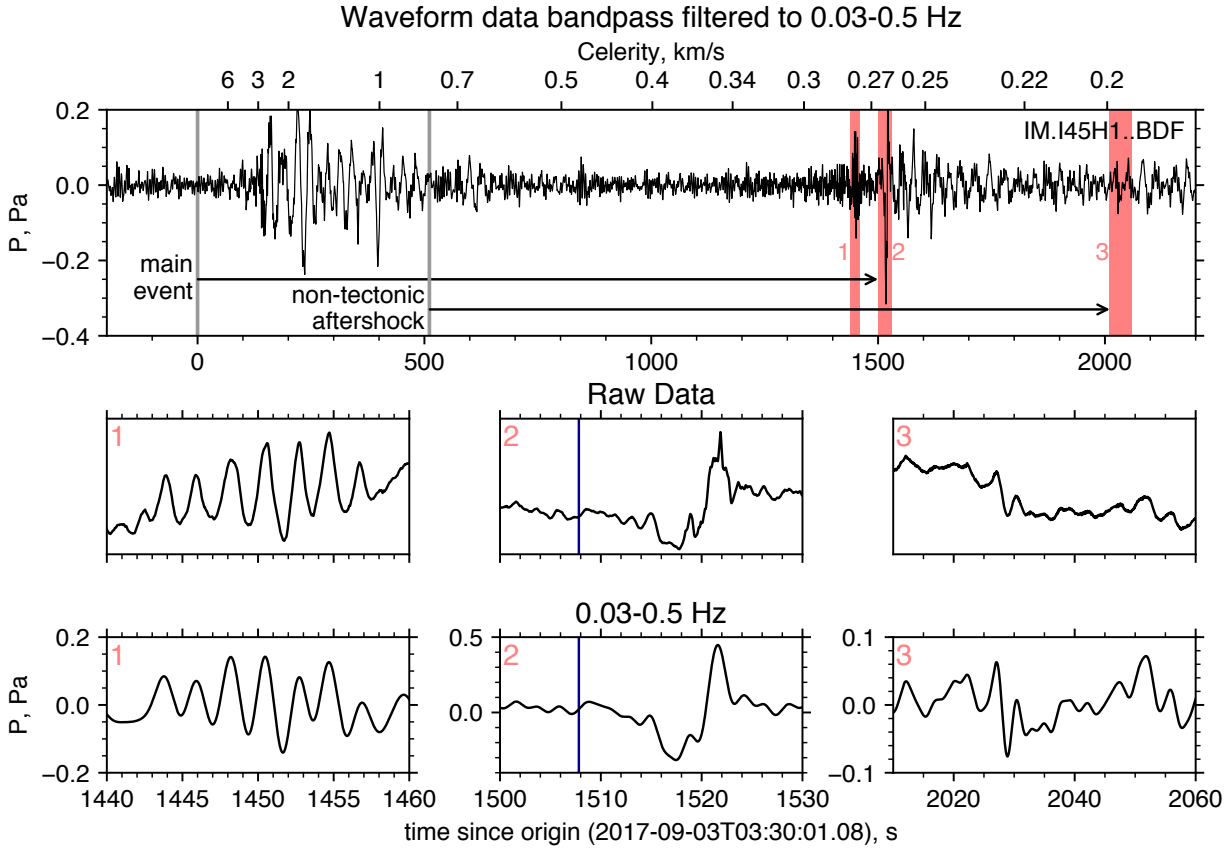

Figure 3: Waveform data from element 1 of IMS array I45US. Top: Bandpass filtered to 0.03-0.5 Hz. 3 time windows marked in red are enlarged in the bottom two rows. Middle: Raw data, and Bottom: Bandpassed. The number at the top-left corner of the middle and bottom frames corresponds to the label next to each of the marked windows in the top frame. Vertical lines at 0, 511, and 1507 (blue) seconds correspond to main event origin time, non-tectonic origin time and calculated time of arrival from ray theory, respectively. Time is in seconds since origin time of the main event. Celerity values with respect to the main event have been added to the top axis.

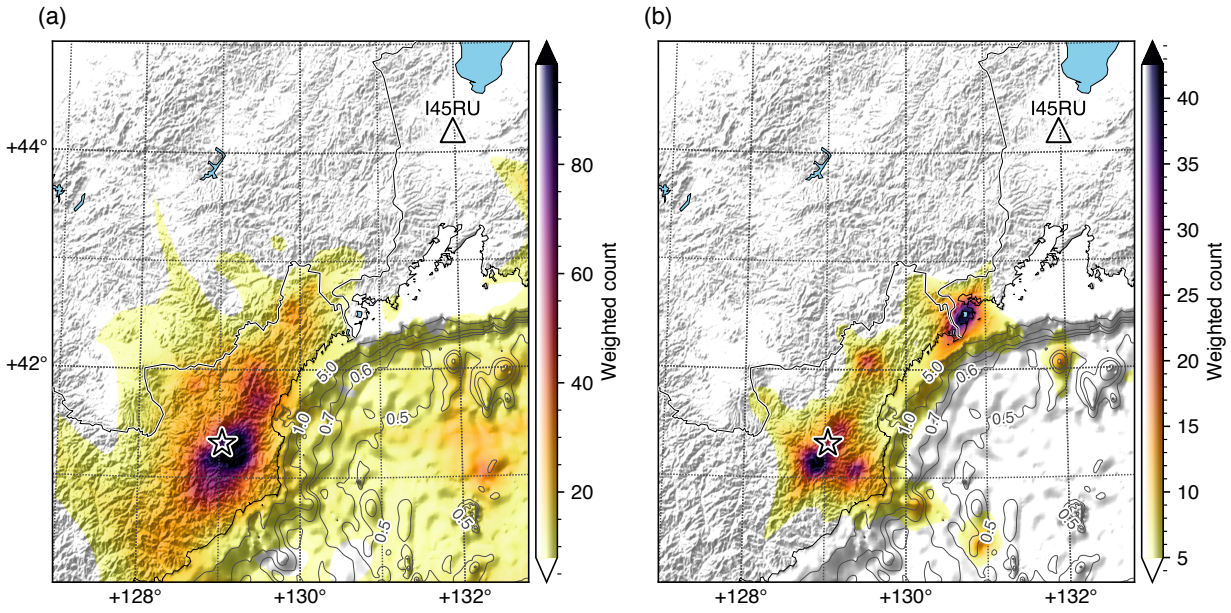

Figure 4: Back-projection results for (a) 0.35-4.0 Hz and (b) 1.0-3.0 Hz frequency bands overlaid on a topography/bathymetry shaded relief (GEBCO 2014 30 arc-second grid, Weatherall et al. (2015)). Contour lines over the bathymetry correspond to water depth of 1 acoustical wavelength at the labeled frequency in Hz. The event location, as listed in the REB, is marked by a star; the I45RU array location is marked by a triangle. Color coding by (SNR) weighted count of detections that originate in each grid cell.

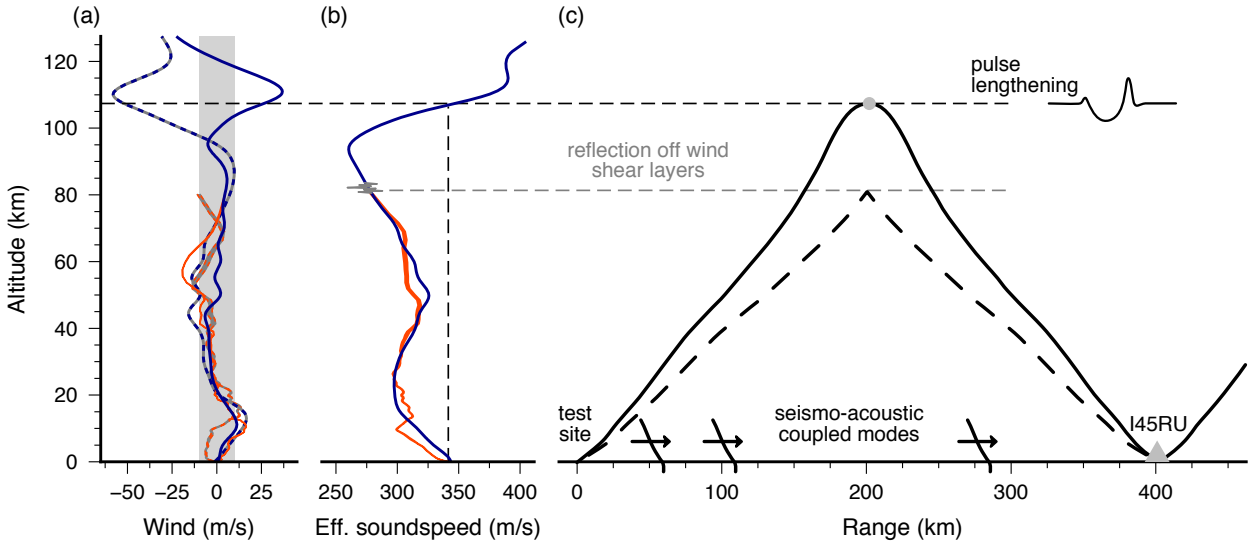

Figure 5: Atmospheric profile at nuclear test site using the ECMWF HRES ensemble of analyses (red, whereas the width indicates the ensemble spread) and HMW14/MSIS-00 climatologies (blue). (a) Along track and crosswind from the test site towards I45RU, indicated by the solid and dashed lines, respectively. Grey area indicates wind velocities of 10 m/s and less. (b) Effective speed of sound approximation in direction of I45RU. A conceptual wind shear layer is added to aid in the understanding of a mechanism for acoustic reflections from mesospheric altitudes. (c) Thermospheric ducting (solid) with caustic (gray circle), simulated by ray theory using the HWM14/MSIS-00 climatologies. Alternative non-resolved paths can be mesospheric returns by reflection off strong wind shear layers (dashed) and seismo-acoustic coupled modes (arrow).

List of Figures

Supplemental information to:

A Seismo-Acoustic Analysis of the 2017 North Korean Nuclear Test

all authors contributed equally.

Jelle Assink,

R&D Seismology and Acoustics, Royal Netherlands Meteorological Institute (KNMI),

P.O. Box 201, 3730 AE, De Bilt, The Netherlands, assink@knmi.nl

Gil Averbuch,

Faculty of Civil Engineering and Geosciences, Department of Geoscience and Engineering,

Delft University of Technology, Stevinweg 1, 2628 CN, Delft, The Netherlands

Shahar Shani-Kadmiel,

Faculty of Civil Engineering and Geosciences, Department of Geoscience and Engineering,

Delft University of Technology, Stevinweg 1, 2628 CN, Delft, The Netherlands

Pieter Smets,

Faculty of Civil Engineering and Geosciences, Department of Geoscience and Engineering,

Delft University of Technology, Stevinweg 1, 2628 CN, Delft, The Netherlands

Läslo Evers,

Seismology and Acoustics, Royal Netherlands Meteorological Institute (KNMI),

P.O. Box 201, 3730 AE, De Bilt, The Netherlands

Faculty of Civil Engineering and Geosciences, Department of Geoscience and Engineering,

Delft University of Technology, Stevinweg 1, 2628 CN, Delft, The Netherlands

I. Using concurrent microbarom signals from Typhoon Sanvu to constrain atmospheric infrasound propagation conditions

During the 2017 North Korean nuclear test, the stratosphere was in a state of transition from summer to winter and the stratospheric vortex was relatively weak. As long-range infrasound propagation is largely conditioned by the strength and the direction of the stratospheric vortex, this implies that propagation from the test site to I45RU may have occurred along unexpected paths. The mode of propagation can be difficult to decipher from the seismo-acoustic signals alone, as is discussed in the article.

To supplement our understanding of infrasound propagation conditions during the test, it can be insightful to analyse concurrent infrasonic signals that were detected at the infrasound array. Indeed, all signals must have propagated through the same atmosphere, albeit from different directions. In particular, continuous signals in the microbarom band (0.1-0.4 Hz) may provide some additional evidence about the mode of propagation, be it stratospheric or thermospheric (Donn and Rind, 1972). It appears that the diurnal amplitude variations are strongly sensitive to the return height. This is a consequence of the interplay between the varying return height due to the atmospheric tides and infrasonic attenuation in the thermosphere. It allows that semi-diurnal amplitude variations are associated with thermospheric ducting, whereas diurnal variations are associated with stratospheric propagation.

In the 1970s, William Donn and David Rind used continuous signals from ocean storms as a means to monitor the state of the upper atmosphere (Donn and Rind, 1972). The method was applied by (Smets and Evers, 2014) to analyze the lifecycle of the 2009 Sudden Stratospheric Warming (SSW).

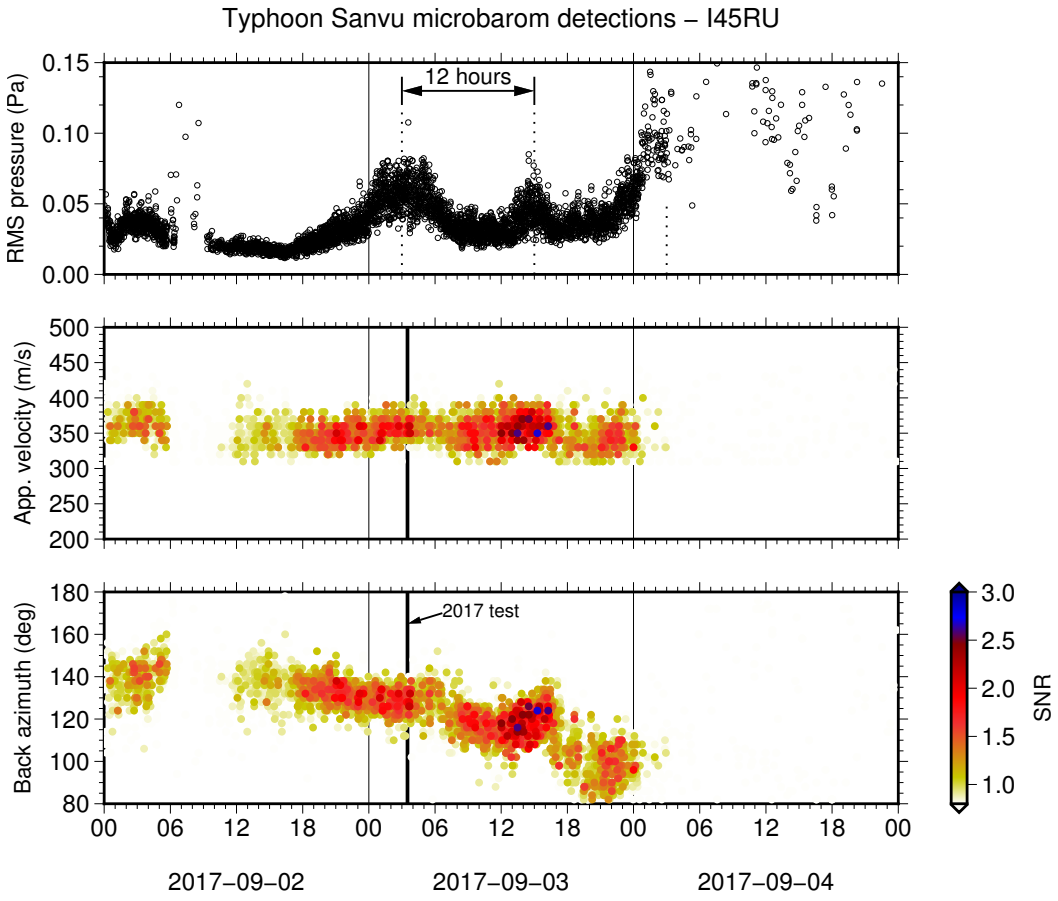

Figure 1: I45RU array processing in the microbarom band (0.1-0.4 Hz) during the first week of September 2017, showing microbarom signals from Typhoon Sanvu. This typhoon was active from 31 August through 3 September 2017 and strong signals were observed during the nuclear test (vertical line). The best beam amplitude shows a semi-diurnal trend that is indicative of thermospheric propagation.

During the 2017 North Korean nuclear test, Typhoon Sanvu was active in the Pacific basin, leading to continuous microbarom observations on array I45RU (Figure 1). The semi-diurnal variation in best beam amplitudes suggest that these signals have propagated through the thermospheric waveguide. This independent observation is in line with the weak stratospheric vortex conditions, as described in the article.

REFERENCES

Donn, W. L. and Rind, D. (1972). Microbaroms and the Temperature and Wind of the Upper Atmosphere. *J. Atmos. Sci.*, 29(1):156–172.

Smets, P. S. M. and Evers, L. G. (2014). The life cycle of a sudden stratospheric warming from infrasonic ambient noise observations. *Journal of Geophysical Research: Atmospheres*, 119(21):12,12–84,99.